Eye-safe compact Raman light detection and ranging temperature profiler

Guangkun Li,[1,5] Geary Schwemmer,[1,2] Coorg Prasad,[2,*] I. H. Hwang,[2] Jie Lei,[2] Sangwoo Lee,[2] Narasimha S. Prasad,[3] and Russell Philbrick[4]

[1]MassTech Inc., 6992 Columbia Gateway Drive, Suite 160, Columbia, Maryland 21046, USA

[2]Science & Engineering Services, Inc., 6992 Columbia Gateway Drive, Suite 200, Columbia, Maryland 21046, USA

[3]NASA Langley Research Center, 5 N. Dryden St., MS 468, Hampton, Virginia 23692, USA

[4]North Carolina State University, Departments of Physics and Atmospheric Sciences (MEAS), Raleigh, North Carolina 27695-8202, USA

[5]Currently at Automated Precision, Inc., 15000 Johns Hopkins Dr., Rockville, Maryland 20850, USA

*Corresponding author: prasad@sesi-md.com

Received 20 August 2013; revised 6 November 2013; accepted 9 November 2013; posted 11 November 2013 (Doc. ID 195998); published 6 December 2013

The vertical profile of atmospheric temperature is a principal state variable to study atmospheric stability. A lidar system, constructed using a 355 nm Nd:YAG laser transmitter, measures the temperature profile using the rotational Raman technique. In comparison with traditional Raman lidar, the major innovations are the use of a low peak power and high repetition rate laser to achieve eye-safe operation in a compact reliable instrument and the use of an angle tuning filter to select operating wavelengths. We demonstrate the capability of both nighttime and daytime measurements as a step toward a future stand-alone capability for routine measurements of important meteorological properties in the lower atmosphere.

OCIS codes: (010.0280) Remote sensing and sensors; (010.3640) Lidar.
http://dx.doi.org/10.1364/AO.52.008540

1. Introduction

The atmospheric temperature profile, which directly determines the environmental lapse rate, is a principal state variable for describing the atmospheric stability. Given the environmental lapse rate, one can estimate the convective activity in the atmosphere. Determining atmospheric stability is important for predicting how the environment will behave under certain conditions. For example, atmospheric stability is a key parameter in forecasting the generation of localized turbulence and the lifetime of aircraft wake vortices, which are the important conditions requiring additional pilot attention during takeoff and landing. The two main reasons for additional concerns related to aircraft operations in the vicinity of airports are (1) relatively slower speed at high angle of attack and low altitudes during takeoff and landing leads to formation of potentially dangerous wingtip vortices, and (2) there are high risks of interference from another aircraft's long-lived wake turbulence [1]. A pilot has little margin for recovery, especially while the aircraft is operating at low speed. Research has shown that the properties of wake vortices, such as their transport and decay, are highly dependent on the local meteorological conditions [2]. Using available data on temperature profiles, eddy dissipation rates, and wind fields, current algorithms can estimate characteristics of wakes generated by specific aircraft types, as well as predict wake upset, based upon the tolerance of an aircraft.

1559-128X/13/358540-09$15.00/0

To date, the rotational Raman lidar technique is the most reliable method for remotely profiling temperature in the troposphere. The rotational Raman technique uses the temperature dependence of the pure rotational Raman scattering line intensities, as was first suggested by Cooney in 1972 [3]. The temperature is determined from the ratios of thermal population distributions of the pure rotational states as described by the Boltzmann distribution, $A(J,T)$; see Eq. (1). The method utilizes the rotational Raman spectrum of molecular nitrogen and oxygen and is independent of other external assumptions about the state of the atmosphere. The ratio of rotational states describes the temperature [3], even in the presence of optical scattering by aerosol and cloud particles, as

$$R(T) = \frac{P_2}{P_1} = \frac{\sum_S \sum_J (N_S * A_S(J,T) * \phi_{2,S}(J) * \sigma(J)}{\sum_S \sum_J (N_S * A_S(J,T) * \phi_{1,S}(J) * \sigma(J)},$$
$$\text{where } A_S(J,T) = \frac{g(J)}{Q(T)}(2J+1) * \exp\left[-\frac{E_J}{KT}\right] \quad (1)$$

and S represents the molecular species, N_S is the species fraction in the atmosphere, P_1 and P_2 represent the signals from first and second filter channels, and $A_s(J,T)$ is each species' thermal population distribution of rotational states at temperature, T, and quantum number, J. The values of $\sigma(J)$ are the rotational Raman scattering cross sections, φ_1 and φ_2 represent the narrowband filter transmission functions, $g(J)$ are the molecular spin statistical weighting factors, E_J is the energy of the Jth quantum state, and $Q(T)$ is the rotational partition function. Based on Eq. (1), the rotational Raman scattering intensity is a function of only molecular properties and temperature. The method to obtain temperature from the rotational Raman spectrum is to measure the ratio of the thermal population distribution of the rotational states $A(J,T)$. Figure 1 shows the spectrum of rotational Raman lines for N_2 and O_2 at two different atmospheric temperatures for excitation at 354.7 nm (the $\Delta J = 0$ line is not included). The differences in intensities at the two temperatures clearly show the relative changes between the low-J (near 354 nm) and the high-J (near 353 nm) lines that provide the signature for the measurement.

Atmospheric temperature measurements using Raman lidar techniques are well established and have been enabled by contributions from several research groups [4–18]. The early steps to prepare for implementation of ways to measure atmospheric temperature profiles occurred from mid-1970s to mid-1980s in several efforts [3–6]. The first significant results for atmospheric temperature profiles using the rotational Raman technique were carried out in the mid-1990s by groups in France [7,8], the UK [9], and the USA [10–12]. A primary issue in

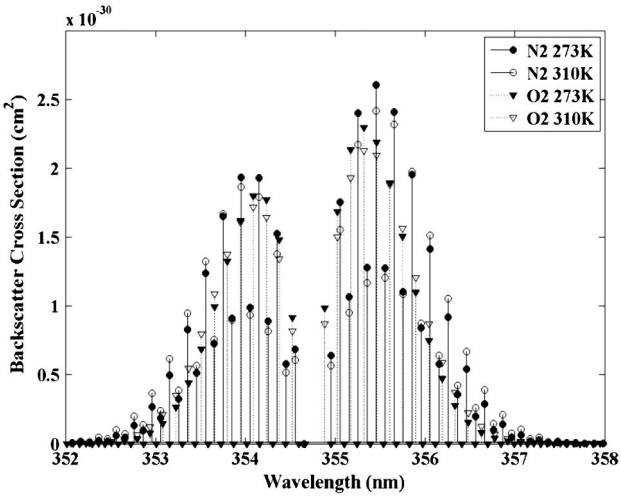

Fig. 1. Spectrum shows the rotational Raman lines for N_2 and O_2 at two different temperatures for excitation at 354.7 nm.

preparing an instrument for these measurements is achieving satisfactory sensitivity with adequate rejection of the backscatter from molecular and aerosol scattering at the transmitted laser wavelength. Many research groups now make use of the technique for atmospheric studies; however, the reason for undertaking this current effort is to develop a low-maintenance and easy to operate instrument that is eye safe, as required in the vicinity of airports. The major innovation of our approach is to use a low-power and high repetition rate laser, instead of the high-power and low repetition rate flash lamp pumped laser systems commonly used for such instruments. This approach allows us to achieve our goal of building an eye-safe, compact, robust, reliable, and low-maintenance instrument. For daytime operation, it is common to use high-energy laser pulses to obtain sufficient lidar signal to overcome the daytime background. A problem with the high repetition rate (~10 kHz) lasers is that their pulse energies are typically significantly smaller than those of the commonly used low repetition (<100 Hz) lasers and thus result in smaller signals than the daytime background. However, we demonstrate by our analysis and experiments that this issue can be overcome with a careful design of the receiver and by utilizing a photon counting detector system.

2. System Setup

Several major innovations are included that are unlike conventional Raman lidar systems. The first of these is to adopt the approach used in a high-sensitivity portable digital lidar successfully implemented in many of our previous Rayleigh lidar systems [19]. Unlike conventional lidar that uses a high-energy laser pulse and a large aperture telescope to obtain adequate backscattered signal, the digital lidar utilizes a high pulse repetition rate (PRF) low-energy laser transmitter, a smaller telescope receiver, and a photon counting detection system to achieve an adequate signal-to-noise ratio

(SNR), even when averaging over a short period of time. The inherent ultralow noise floor of photon counting detectors, such as channel photomultipliers or photomultiplier tubes (PMTs), allows the much smaller laser pulse energy digital lidar system to provide performance comparable to the high laser pulse energy systems by summing many smaller returns without adding detector noise, provided background noise can be sufficiently minimized. Diode pumped solid state lasers that are optimally suited for high repetition rate operation enable the reduction in laser pulse energy. The laser used in this instrument is an Nd:YAG laser (Coherent AVIA 355-7000 UV) that emits UV pulses at 354.7 nm with an average power of ~4 W at a 10 kHz repetition rate. Its output is fiber coupled to the transmitter. The average power and pulse energy after all the transmitter optics are approximately 1.5 W and 150 μJ, respectively. Figure 2 shows the schematic diagram of the instrument.

The transmitting and receiving optics are separated into two separate telescopes for convenience in moving the instrument and to make it easier to assemble and align the instrument. The UV laser beam is fiber coupled to a 7.5 cm telescope as the lidar transmitter. A 32 cm Cassegrain telescope is used as the main receiver. The telescope focuses the collected light through a 0.6 mm pinhole to remove stray light, and the signal is collected by an optical fiber, which transfers it to a dichroic beam splitter, and passes the signal to the two Raman filter channels. One of the filter channels is for the low J-level (stronger Raman scattering) and the other is for high J-level (weaker Raman scattering) channels. A third, 10 cm diameter telescope, located on the side of the main telescope, receives the 354.7 nm elastic backscatter signal that provides a Rayleigh lidar signal. Even though this UV elastic channel is not essential for the Raman temperature measurement,

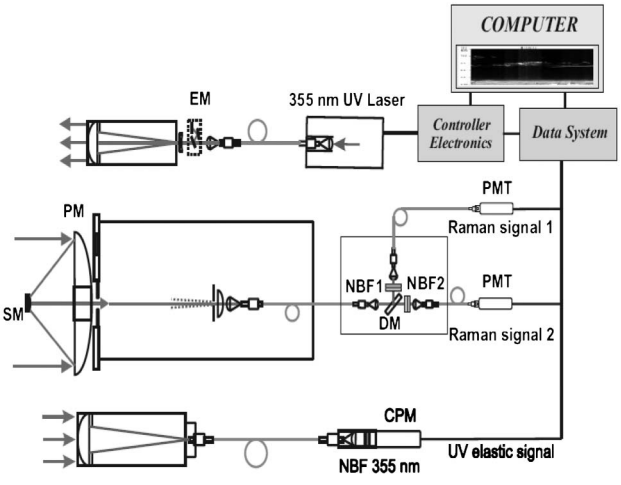

Fig. 2. Schematic of the Raman lidar system: EM, energy monitor; PM and SM, primary and secondary telescope mirrors with pinhole near the focus; NBF, narrowband filters; DM, dichroic mirror; PMT, photomultiplier tubes; and CPM, channel photomultiplier.

it is very useful as a reference to monitor the atmospheric aerosol profile and obtain aerosol optical extinction measurements [20].

The experimental technique usually involves inserting two narrowband Raman filters that are specified for selected wavelengths in either of the anti-Stokes or Stokes bands of the rotational Raman spectrum shown in Fig. 1. Since the spectrum changes with changing temperature, the ratio of the two signals is analyzed to retrieve the temperature profile. In order to avoid possible signal contamination from fluorescence, we selected the anti-Stokes spectrum. The N_2 and O_2 rotational Raman signal components are summed and integrated over the narrow transmission band of the two spectral filters. It is only necessary to include the N_2 and O_2 rotational Raman lines in the analysis because the possible interfering signals (water vapor and aerosol scatter, ozone absorption, and the background radiation) are either spectrally flat over the range of a few nanometers or are small contributors to the signals within the filter bandwidths.

This study demonstrates temperature measurements using angle tuning of relatively low-cost standard laser line filters, instead of custom wavelength narrowband filters. A primary technical challenge of the rotational Raman system is to achieve sufficiently high rejection of the elastic backscattering signal from the rotational Raman channels. The scattering line intensities of rotational Raman are typically 4 orders of magnitude lower than the elastic Mie and Rayleigh scattering intensities. Even though several rotational lines are included within the band, the rejection of elastic scattering signals by the Raman filters should be greater than $\sim 10^6$ to permit measurements at 1% accuracy in the presence of elastic scattering from molecules and aerosols. These Raman filters are required to transmit narrow bands of wavelengths centered at our selected wavelengths and have sufficiently high rejection of the elastic backscattering signal at 354.66 nm; also they must reject the integrated signal of the remaining broad wavelength background, when sky light intensity and detector sensitivity are high. Thus, the major technical challenge of a rotational Raman lidar system is to achieve good transmission in the selected bands, combined with sufficiently high out-of-band rejection of the broadband skylight, the molecular Cabannes line ($\Delta J = 0$), and the aerosol scatter [21].

We use a set of narrowband laser line interference filters centered at 354.66 nm at normal incidence with 0.2 nm full width at half-maximum (FWHM) bandwidth. We are able to shift the central wavelength to the anti-Stokes region by wavelength tuning with the incidence angle of light,

$$\lambda_c = \lambda_0 \sqrt{1 - \sin^2 \theta / n^2}, \tag{2}$$

where θ is the filter incident angle and n is the filter's effective refractive index. By angle tuning the filter

to 5° and 8.3°, we were able to set the central wavelengths of the narrow bands to 354 and 353 nm, respectively. Based upon our measurements, the rejection rate we are able to obtain from a single filter is an optical density (OD) ~3.5 (~3×10^{-4} transmission). This is significantly less than the needed OD ~6. We solve this problem by combining two filters in series to double the laser line OD and thereby achieve an OD ~7 rejection rate in each channel.

Table 1 summarizes the performance for the low J-level (Filter 1) and high J-level (Filter 2) doubled filters used in this investigation. The transmission curve for the filter was obtained from the vendor, and it is verified using a laboratory spectrometer; additionally an outdoor test providing experimental verification is reported.

Table 2 provides the system characteristics. Although measurements are acquired with 0.25 s time step and 9.375 m range resolution, the received signal is typically integrated for a longer time and a coarser range resolution during analysis to improve the SNR, prior to calculating temperatures.

3. Ratio Calibration and Error Analysis

We explored two different approaches to calculate temperature from the ratio of two rotational Raman signals. In the first method, we used theoretical calculations to establish a lookup table (LUT) between the ratio of band transmissions and temperatures calculated using Eq. (1). Each Raman lidar system has its own temperature-dependent ratio curve, which can be determined by using the system hardware parameters. Given the lidar characteristics in Tables 1 and 2, the signal returns of the two rotational Raman channels are calculated based upon the detector parameters, the convolution of the filter functions with the rotational Raman cross sections, and the fractional composition of air. Figure 3 shows the ratio of the two Raman channels calculated for our lidar system. Note that Q is also sensitive to the specific filter wavelengths and spectral characteristics.

Using the second method, we apply a least squares fit of the lidar rotational Raman ratio data to balloon radio sonde temperature data, as first proposed by Nedeljkovic *et al.* [8]. This model was further developed and simplified by Haris and Philbrick [11] and Balsiger *et al.* [12], using the assumption that a second-order polynomial model relates the temperature, T, to the lidar signal ratios, R, in the form

$$T = C_0 + C_1 R + C_2 R^2. \tag{3}$$

Given the ratio of the lower J-level and higher J-level rotational Raman channels, we can estimate the 1 – σ statistical temperature uncertainty from differentiating Eq. (1):

$$\Delta T = \frac{\partial T}{\partial R}\Delta R \approx \frac{(T_1 - T_2)}{(R_1 - R_2)} R_1 \sqrt{(P_1 + P_{B1})/P_1^2 + (P_2 + P_{B2})/P_2^2}, \tag{4}$$

where P_1 and P_2 represent the rotational Raman signals without background, P_{B1} and P_{B2} represent the solar background radiation, T_1 and T_2 represent temperature pairs used in the calculation, and R_1 and R_2 represent the ratios of the rotational Raman channels for the two temperatures [11]. The estimated sensitivity curves are shown in Fig. 4 for night and in Fig. 5 for daytime measurements.

Table 1. Specifications of the Low-J and High-J Band Filters

	Filter 1 (Low-J)	Filter 2 (High-J)
Wavelength	353.95 nm	352.9 nm
Tuning angle	5°	8.3°
FWHM	0.2 nm	0.2 nm
Peak transmission	>15%	>15%
Laser line transmission	$<7 \times 10^{-8}$	$<2 \times 10^{-8}$

Table 2. Raman Lidar Breadboard Characteristics

Transmitter	
Wavelength	354.66 nm
Laser	Coherent AVIA 355-7000 third-harmonic Nd:YAG
Repetition rate	10,000 Hz
Energy per shot	150 μJ
Output beam Divergence	Diameter 7.62 cm 250 μrad (half-angle)
Receiver	
Telescope diameter	30.5 cm
Field of view	300 μrad (half-angle)
Focal length	2 m
Time resolution	0.25 s
Range resolution	9.375 m
Detection	Photon counting (PMT)

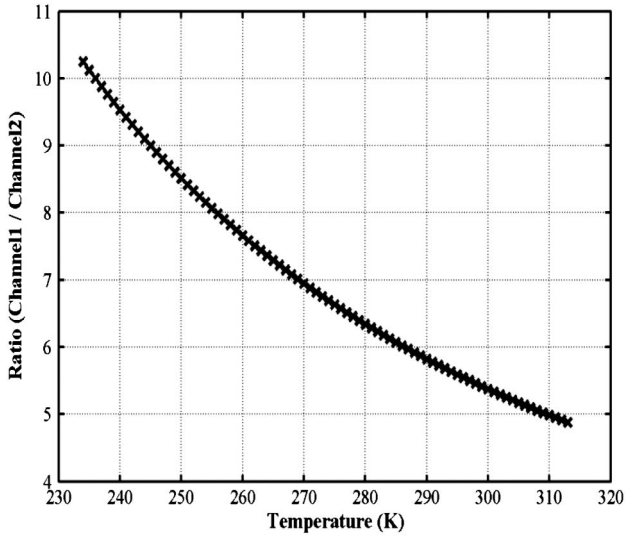

Fig. 3. Calculation shows the ratio of the lower J-level over the higher J-level rotational Raman channels as a function of temperature.

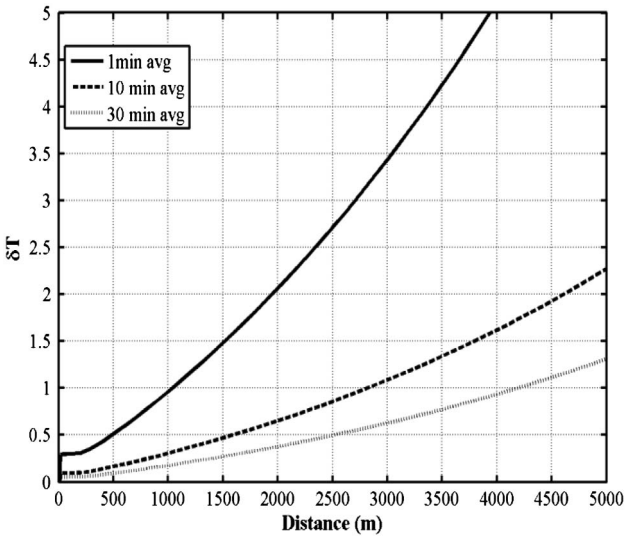

Fig. 4. Estimate of the nighttime $(1-\sigma)$ sensitivity curve of the Raman lidar.

The analysis indicates that we are able to achieve 1 K accuracy for 10 min average at nighttime below 3 km. The daytime solar background for a high solar angle is estimated using a MODTRAN simulation [22] and corresponds to ~3 photon counts/μs received signal in our system. During daytime, even in the extreme cases, we are able to achieve ~3.5 K accuracy below 1 km for 30 min integration and 100 m range resolution. We expect much better performance in an improved version of the instrument, which will use a narrower field-of-view receiver to further reduce the sky background, a higher power laser, and an improved instrument design to increase optical transmission efficiency.

4. Results

A breadboard lidar system was assembled to measure rotational Raman backscatter signals during both daytime and nighttime. It is pointed vertically, while profiles are collected with integration time intervals from 0.25 to 30 s. The Raman signals are measured using two Hamamatsu Model H6180-01 PMTs after passing through a dichroic beam splitter and the narrowband filters.

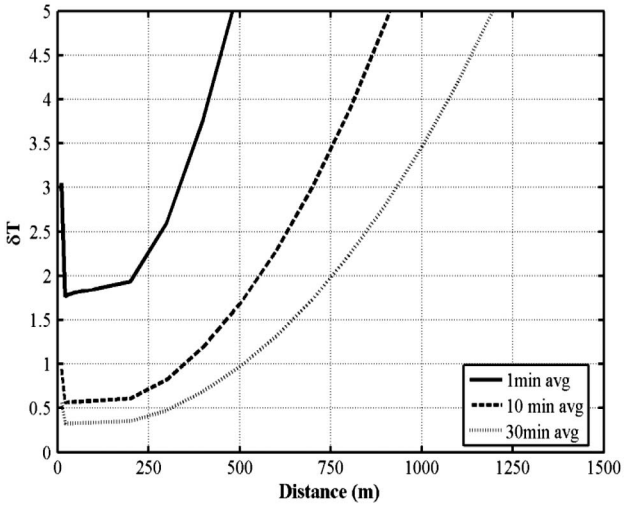

Fig. 5. Estimate of the $1-\sigma$ daytime sensitivity curve of the Raman lidar.

A. Blocking of the Laser Line

As mentioned above, the major technical challenge of our Raman lidar system is to ensure sufficiently high blocking of the strong elastic backscattering signal from the rotational Raman channels. To verify that we achieve >OD of 6 blocking on both filter channels, an experiment is carried out on a cloudy night to examine the signal return from rotational Raman channels and compare it with the reference UV elastic channel.

Figure 6(a) shows the raw data profiles from three channels; lower J-level, higher J-level, and elastic $(\Delta J = 0)$ channel. This plot shows measurements obtained in a 10 min integration time and a 9.375 m range resolution, when the beam intentionally hits a cloud layer. An elastic backscatter return signal of ~3 counts/μs is observed from the cloud layer at 2.5 km, but no evidence of any interference in the signal returns is observed from the two rotational Raman channels at the cloud location, even when we examine the scale at 10^{-5} counts/μs signal level. Considering that the receiving efficiency of the UV elastic channel is approximately 9 times less than the rotational Raman channels, due primarily to the smaller telescope area (10 cm versus 30.5 cm diameter), and the offset in the alignment of the elastic receiver (the laser beam is primarily aligned with

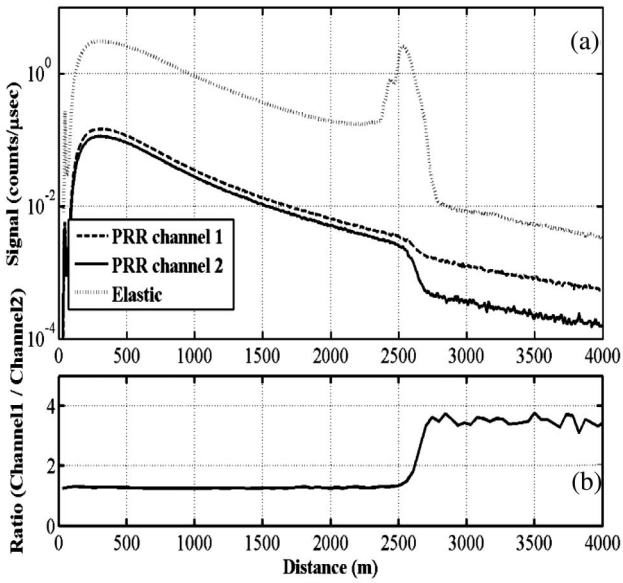

Fig. 6. Lidar returns on 12 April 2012 (near 10 p.m.) are plotted when the beam intentionally hit a cloud layer near 2.5 km. (a) Average for 10 min profiles of the three raw data returns, and (b) ratio of the high-J divided by low-J values shows a significant temperature drop across the cloud (filter wavelengths in this test are not those in Table 1 that are used in the LUT calculation shown in Fig. 3).

the 30.5 cm receiver), we estimate that the UV blocking of the two Raman channel filters is greater than OD = 7. One interesting observation from Fig. 6 is that a significant change occurs in the ratio of the two Raman channels in passing through the cloud layer [see Fig. 6(b)]. The profiles show that the atmosphere is significantly warmer below the cloud and rapidly cools at the cloud top. The relatively constant smaller ratio below the cloud is expected for the heat trapping that is characteristic of extended nighttime cloud cover. The temperature gradients in the near isothermal region below the cloud and the free troposphere, typically ~5.5°C, are too small to show observable difference in the resolution of Fig. 6(b); however, the temperature change in passing through the cloud is striking. The measured values of signal ratios shown here are much smaller than the calculated ratios presented in Fig. 3; the difference is because the final filter wavelength setting described in Table 1 had not yet been selected.

Figure 7 shows the measured rotational Raman signal returns compared as a function of wavelength with those expected for the molecular Raman $N_2 + O_2$ rotational Raman line strength peaks. This test is accomplished by shifting the central wavelength of one Raman channel by angle tuning of the filter. The wavelength is stepped by changing the incidence angle of light passing through the interference filter. The central wavelength of the filter is tuned from 352.1 to 354.2 nm in small steps, during this experiment, when the atmosphere appeared to be stable, between 9:00 and 10:30 p.m. on 30 April 2012. At each wavelength, the lidar return signals are integrated for 3 min and then compared with the integrated contribution of the rotational Raman cross sections at the wavelengths within the filter range, after accounting for the relative composition of N_2 and O_2.

The bars in Fig. 7 represent the relative values for the Raman scattering cross-section contribution from $O_2 + N_2$ compared with the measured intensity points on the line, which shows that the measured rotational Raman lidar signals as a function of the stepped wavelength agree very well. The lidar signals at each wavelength are obtained by integrating the raw data over the altitude range 400–900 m for three 1 min time periods. We can also confirm that blocking of the strong elastic backscatter returns is also achieved during this test by hitting a cloud layer near 1.2 km (above the altitude used in preparing Fig. 7). Again, we did not observe any interfering return in the Raman channels for wavelengths less than 354.2 nm (i.e., 0.5 nm from the laser wavelength). At longer wavelengths, the elastic backscatter signal does begin to contaminate the rotational Raman signal as we approach the laser line at 354.66 nm, there by further supporting our conclusion that the narrowband filter provides sufficient blocking of the elastic signal when the center wavelengths are more than about 0.5 nm from the laser line.

B. Night-time Temperature Measurement and Calibration

The temperature profile is first calculated using the LUT method, which is based upon the calculation using the parameters for the assembled hardware components of the instrument. The LUT calculation curve is shown in Fig. 3. Using the LUT, we were able to convert the measured ratio of the two channels to find the values for the atmospheric temperature profile; these results are shown in Fig. 8(a). All of the results reported after 1 May 2012 are obtained under

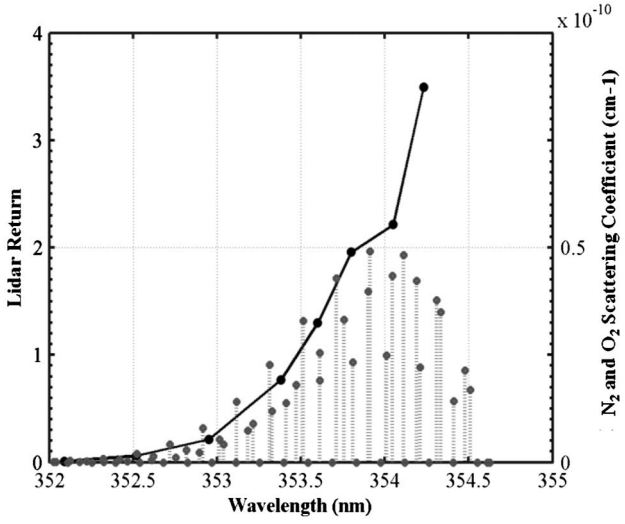

Fig. 7. Integrated raw data from 500 to 900 m at various wavelengths compared with rotational Raman scattering for N_2 and O_2 in air, 9–10 p.m. on 30 April 2012. Note the separation of the signal from the coefficients when the filter central wavelength (354.2 nm) moves too close to the laser line (354.66 nm).

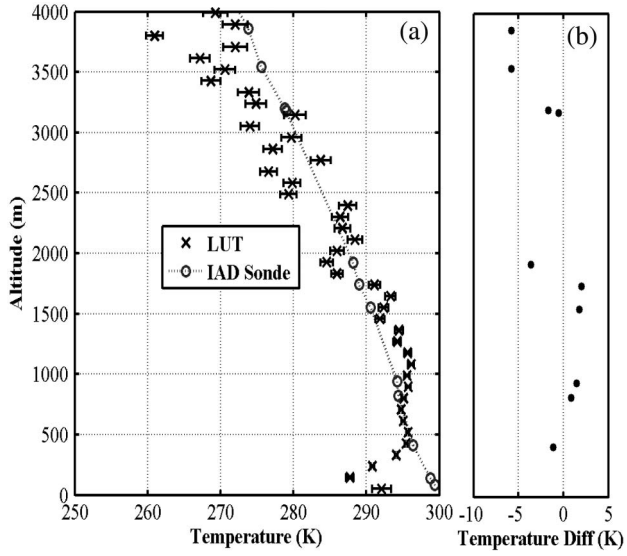

Fig. 8. Lidar and IAD rawinsonde measurements on 3 May 2012. (a) Comparison between sonde (taken at 8 p.m.) and 1 h average (between 8:31 and 9:30 p.m.) Raman lidar temperature profiles when retrieved using a LUT, and (b) temperature difference between lidar and sonde.

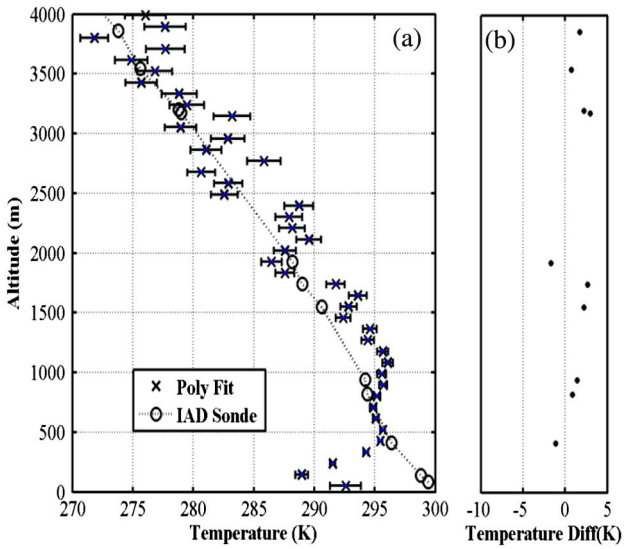

Fig. 9. Lidar and IAD rawinsonde measurements on 3 May 2012. (a) Comparison between sonde and Raman lidar temperature profile using a quadratic polynomial fit of the rawinsonde data, and (b) temperature difference of lidar minus sonde temperature. Note that the temperature scale in Fig. 8 is different from that in Fig. 9.

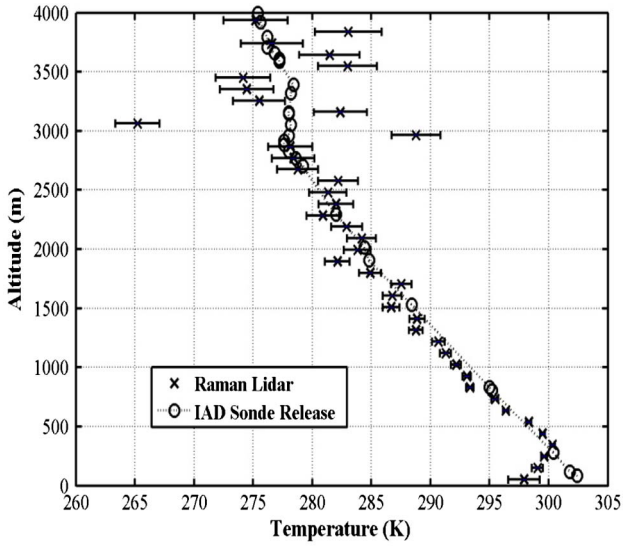

Fig. 10. Raman lidar temperature profile compared with the IAD rawinsonde measurement on 12 August 2012 7:45–8:45 p.m.

conditions corresponding to the parameters of Tables 1 and 2 and therefore are well represented by the calculation shown in Fig. 3. Raman temperature data averaged between 8:31 and 9:30 p.m., with standard deviation error bars, are shown in Fig. 8(a). The line connects the data points reported for the rawinsonde balloon measurements of the temperature for a release near Dulles International Airport (IAD) at 8 p.m. (obtained from public database). It is not an ideal comparison for our lidar temperature profile because (1) the rawinsonde release is over an hour earlier, near local sunset, and (2) the release site is 39 miles away from our test site; however, the two data sets do generally agree within ±2 K up to 3.5 km. Figure 8(b) shows the temperature difference by subtracting the sonde temperature from the interpolated lidar temperature between 300 and 4000 m. The standard deviation of the difference is ~3 K.

It is difficult to achieve an ideal scenario to compare the measured data to an independent measurement of temperature needed to verify the ratio curve of a specific lidar system. The approach that has provided the better performance uses the second-order polynomial fit method [11,12]. Figure 9(a) shows the comparison using this analysis method for the same data and time period as shown in Fig. 8. Figure 9(b) indicates that the least squares fit method shows better agreement between lidar data and the rawinsonde data, with a standard deviation of ~1.5 K. In summary, the comparisons between Raman lidar and rawinsonde balloon measurements show good agreement. The Raman lidar profile has more measurement points (40 versus 10 data points available for the sonde below 4 km), and it exhibits higher spatial resolution temperature structure.

Figure 10 shows another Raman lidar measurement (soon after sunset) on 12 August 2012 from 7:45 to 8:45 EDT. The comparisons between the lidar and the IAD rawinsonde measurement at 8 p.m. show closer agreement than in the 3 May data shown in Figs. 8 and 9. These data were taken near sunset, when there is still a significant amount of twilight background present. These data were taken during the time of sunset shown in Fig. 11 to provide the overlap with the balloon release, but we are able to obtain better than 2 K accuracy up to 3 km during the 1 h average. The analysis is performed using the same second-order polynomial with the coefficients determined for the earlier experiment shown in Fig. 9. Once the fit parameters for the second-order polynomial are determined, they are found to be

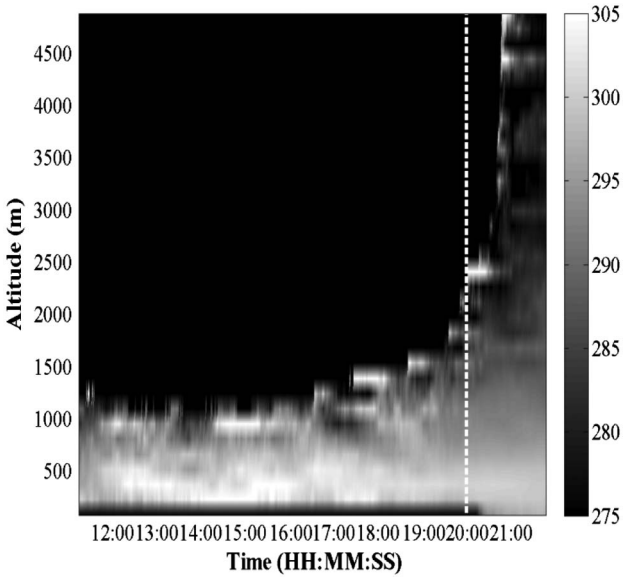

Fig. 11. Time series temperature profiles show data taken on 12 August 2012 11 a.m. to 10:30 p.m. (vertical line indicates the sunset time). Notice the smoothing of the boundary layer structure after sunset.

useful until a significant instrument modification is made.

C. Daytime Temperature Measurement

To observe the daytime performance, measurements were obtained from morning (around 10 a.m.) through sunset for a period of a few days with different environmental conditions, such as cloudy and clear days. Figure 11 shows a false color plot of the time series measurement of the temperature profile on 12 August 2012 from 10 a.m. to 9:30 p.m., which includes the data period shown in Fig. 10. In this extended data set, the temperature profile is calculated with 100 m range resolution. The data are also analyzed using a 15 min moving average in time, and the results are cut at a SNR = 20 threshold, which corresponds to approximately 5 K accuracy in temperature. The color (or gray-scale) represents variation from approximately 275–305 K, as shown in the scale on the right side. As expected, Fig. 11 shows that the measurement sensitivity increases markedly when the solar background decreases. At noontime, when the solar background is at its peak, we were able to achieve 5 K accuracy below 1.1 km, while at nighttime, the altitude range with 5 K accuracy increases to above 4 km.

5. Conclusion and Outlook

We report the development of an eye-safe Raman lidar temperature profiler for measuring daytime and nighttime temperature profiles in the lower troposphere using the rotational Raman method. Atmospheric temperature measurements using Raman lidar techniques are well established and implemented by several research groups. However, problems with these systems include complexity and high maintenance. The major innovations of our approach combine a low-energy, high PRF laser and a highly effective rotational Raman filter arrangement. It is used to demonstrate the capabilities and potential of an eye-safe, compact, robust, reliable, and low-maintenance instrument.

Using the Raman lidar, we demonstrate the capability of performing high-sensitivity nighttime temperature measurements, achieving accuracy of 1 K with vertical resolution of 100 m at 3 km in 10 min measurement intervals. We have demonstrated that narrowband laser line optical filters can effectively be used as Raman channel filters and also that a low-energy (a few 100 μJ per pulse), high-repetition rate laser is able to overcome the daylight background.

We are exploring various possibilities to further improve the daytime performance of the system. One of the issues we observed during the laboratory and outdoor measurements is the quality of the UV laser beam sent through the small telescope. Based upon our calculation, we should be able to increase the SNR by more than 5 times by reducing the laser beam divergence and the field of view. In addition, with better beam collimation, a smaller field of view in the receiver will be used to reduce the daylight background. We plan to implement other improvements to (1) optimize the Raman filters, (2) improve beam quality to reduce divergence and increase the laser power, and (3) redesign receiver optics to reduce the field of view and lower the stray light. With all these improvements, we expect to significantly improve the daytime performance of the Raman lidar and achieve continuous profiling for both daytime and nighttime conditions.

The authors gratefully acknowledge funding under a NASA SBIR Phase I program entitled Raman Lidar Temperature Profiler, contract no. NNX12CF29P.

References

1. S. I. Green, "Wing tip vortices," in *Fluid Vortices: Fluid Mechanics and Its Applications*, S. I. Green, ed. (Springer, 1995), pp. 427–470.
2. J. N. Hallock, G. C. Greene, and D. C. Burnham, "Wake vortex research: a retrospective look," Air Traffic Control Q. **6**, 161–178 (1998).
3. J. Cooney, "Measurement of atmospheric temperature profiles by Raman backscatter," J. Appl. Meteorol. **11**, 108–112 (1972).
4. H. Inaba, "Detection of atoms and molecules by Raman scattering and resonance fluorescence" in *Laser Monitoring of the Atmosphere*, Volume 14 of Topics in Applied Physics, E. D. Hinkley, ed. (Springer, 1976), pp. 153–236.
5. J. A. Cooney, "Uses of Raman scattering for remote sensing of atmospheric properties of meteorological significance," Opt. Eng. **22**, 292–301 (1983).
6. Y. F. Arshinov, S. M. Bobrovnikov, V. E. Zuev, and V. M. Mitev, "Atmospheric temperature measurements using a pure rotational Raman lidar," Appl. Opt. **22**, 2984–2990 (1983).
7. M. L. Chanin, A. Hauchecorne, and D. Nedeljkovic, "Temperature measurement by rotational Raman lidar," Proc. SPIE **1714**, 242–250 (1992).
8. D. Nedeljkovic, A. Hauchecorne, and M. L. Chanin, "Rotational Raman lidar to measure the atmospheric temperature from the ground to 30 km," IEEE Trans. Geosci. Remote Sens. **31**, 90–101 (1993).
9. G. Vaughan, D. P. Wareing, S. J. Pepler, L. Thomas, and V. Mitev, "Atmospheric temperature measurements made by rotational Raman scattering," Appl. Opt. **32**, 2758–2764 (1993).
10. C. R. Philbrick, "Raman lidar measurements of atmospheric properties. Atmospheric propagation and remote sensing III," Proc. SPIE **2222**, 922–931 (1994).
11. P. A. T. Haris and C. R. Philbrick, "Rotational Raman lidar for temperature measurements in the troposphere," in *Proceedings of the IEEE Topical Symposium on Combined Optical-Microwave Earth and Atmosphere Sensing*, ID TW.7 (IEEE, 1995), pp. 141–144.
12. F. Balsiger, P. A. T. Haris, and C. R. Philbrick, "Lower tropospheric temperature measurements using a rotational Raman lidar," Proc. SPIE **2832**, 53–60 (1996).
13. I. Balin, I. Serikov, S. Bobrovnikov, V. Simeonov, B. Calpini, Y. Arshinov, and H. Van Den Bergh, "Simultaneous measurement of atmospheric temperature, humidity, and aerosol extinction and backscatter coefficients by a combined vibrational pure-rotational Raman lidar," Appl. Phys. B **79**, 775–782 (2004).
14. A. Behrendt, "Temperature measurements with lidar," in *Lidar: Range-Resolved Optical Remote Sensing of the Atmosphere*, C. Weitkamp, ed. (Springer, 2005), pp. 273–305.
15. C. R. Philbrick, "Raman lidar characterization of the meteorological, electromagnetic and electro-optical environment," Proc. SPIE **5887**, 58870 (2005).
16. M. Radlach, A. Behrendt, and V. Wulfmeyer, "Scanning rotational Raman lidar at 355 nm for the measurement of tropospheric temperature fields," Atmos. Chem. Phys. **8**, 159–169 (2008).

17. J. Reichardt, U. Wandinger, V. Klein, I. Mattis, B. Hilber, and R. Begbie, "RAMSES: German meteorological service autonomous Raman lidar for water vapor, temperature, aerosol, and cloud measurements," Appl. Opt. **51**, 8111–8131 (2012).
18. R. K. Newsom, D. D. Turner, and J. E. M. Goldsmith, "Long-term evaluation of temperature profiles measured by an operational Raman lidar," J. Atmos. Ocean. Technol. **30**, 1616–1634 (2013).
19. H. S. Lee, I. H. Hwang, and C. R. Prasad, "Portable digital lidar system," U.S. patent 6,593,582 B2 (15 July 2003).
20. G. Li and C. R. Philbrick, "Lidar measurements of airborne particulate matter," Proc. SPIE **4893**, 94–104 (2003).
21. A. T. Young, "Rayleigh scattering," Appl. Opt. **20**, 533–535 (1981).
22. A. Berk, G. P. Anderson, P. K. Acharya, L. S. Bernstein, L. Muratov, J. L. Marsha, J. Fox, S. M. Adler-Golden, J. H. Chetwynd, M. L. Hoke, R. B. Lockwood, T. W. Cooley, and J. A. Gardner, "MODTRAN5: a reformulated atmospheric band model with auxiliary species and practical multiple scattering options," Proc. SPIE **5655**, 88–95 (2005).